Intra-operative 3D micro-coil imaging using subsampled tomographic acquisition patterns on a biplane C-arm system

Charlotte Delmas, Cyril Riddell, Yves Trousset, Erwan Kerrien, Marie-Odile Berger, René Anxionnat, Serge Bracard

Intra-operative 3D micro-coil imaging using subsampled tomographic acquisition patterns on a biplane C-arm system

Charlotte Delmas[1,2], Cyril Riddell[1], Yves Trousset[1], Erwan Kerrien[2,3], Marie-Odile Berger[2,3], René Anxionnat[4] and Serge Bracard[4]

***Abstract*—The restriction of CBCT to micro-coil imaging allows for integrating key a priori knowledge that a coil is a high-density spatially sparse curvilinear structure. In this paper, we investigate acquisition patterns specifically designed for biplane systems allowing a faster workflow and reduced dose. Each pattern is a subsampling of a standard tomographic acquisition reconstructed with an ℓ_1-constrained algorithm to promote sparsity together with diffusion filters that promote the curvilinear nature of the coil. Three tensor-based 3D diffusion filters are investigated. Quantitative and qualitative results are provided for one coil and four patients datasets. They show how the reconstruction performs according to the selected acquisition pattern (uniform versus non-uniform subsampling), the quantity of missing information and the selected diffusion filter. We observed a systematically better recovery of the coil in reconstructions obtained using a uniform subsampling pattern but at the cost of being systematically noisier than those obtained with a non-uniform subsampling pattern. Diffusion filtering significantly reduced this structural noise.**

I. Introduction

Endovascular aneurysm coiling is a minimally invasive procedure most commonly used for treating balloon-shaped cerebral aneurysms. A micro-coil (or coil) is a pre-shaped platinum wire that is guided through a catheter inside the aneurysm and that winds as it exits the catheter. Several coils are usually placed one after the other to embolize the aneurysm, thus preventing blood from pressuring the diseased vessel wall and starting an hemorrhage. Real-time guidance and control are obtained using fluoroscopic images acquired with an X-ray biplane C-arm system (Fig.1). Proper positioning of the coils means that no coil loop should enter the parent artery. However, some anatomical configurations of aneurysms require moving the C-arm in positions that are not available due to mechanical restrictions. In such cases, Cone-Beam Computed Tomography (CBCT) provides a 3D depiction of the coil. In the standard CBCT workflow, the X-ray source of the frontal plane of the C-arm rotates over a 200° circular arc (called spin). The lateral plane must be parked prior to the acquisition and repositioned after so that performing

Authors are with : 1/ GE Healthcare, Buc, France, 2/ Loria, Vandœuvre-lès-Nancy, France, 3/ Inria, Vandœuvre-lès-Nancy, France, 4/ Centre de Neuroradiologie du CHU de Nancy, France. Corresponding author: cyril.riddell@ge.com. This work was supported by the CIFRE grant No. 2012/1280 from the French Association Nationale de la Recherche et de la Technologie (ANRT).

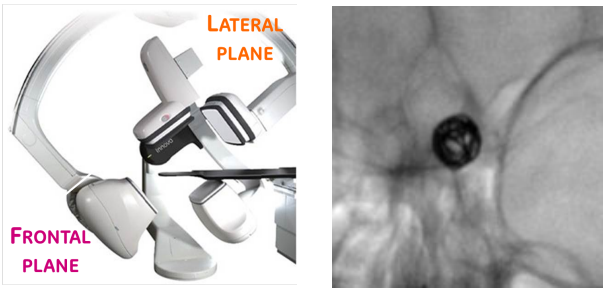

(a) (b)

Fig. 1. (a) GE Healthcare IGS 630 biplane acquisition system. (b) X-ray projection of a single intra-cranial micro-coil

CBCT is time-consuming. It is also expensive in terms of X-ray dose to the patient with respect to fluoroscopy. Our purpose is thus to investigate angularly subsampled rotational acquisition patterns that are appropriate for intra-operative 3D coil imaging by taking advantage of the knowledge that the object of interest is a coil.

II. Methods

The restriction of CBCT to coil imaging allows for integrating key a priori knowledge of the object of interest: it is a high-density spatially sparse curvilinear structure. Recently developed compressed-sensing-based CBCT reconstruction algorithms have shown promise for reconstructing sparse objects [1]. In our context, we consider a reconstruction algorithm constraining the ℓ_1-norm of the image to promote sparsity together with diffusion filters to also promote curvilinear structures. We here discuss several subsampling schemes of the standard CBCT acquisition designed such that the lateral plane needs not be parked and compare uniform versus non-uniform subsampling.

A. Subsampling patterns

Fig.2 illustrates the three angularly subsampled acquisition patterns that are investigated. Pattern P_0 corresponds to the case where the lateral plane is left in place but not used. The frontal plane angular coverage is thus restricted. It is a limited-aperture tomographic acquisition. Within the aperture limits, the angular sampling is uniform and equal to that of a standard

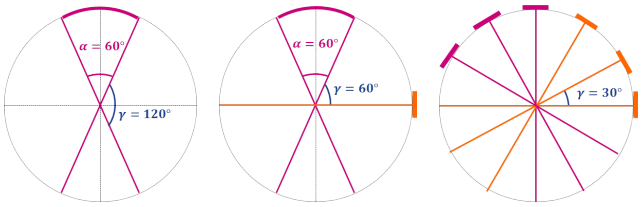

(a) (b) (c)

Fig. 2. Acquisition patterns: (a) P_0 is a limited-aperture rotation (aperture angle $\alpha = 60°$), (b) P_1 adds one extra-projection to P_0, (c) P_2 is a uniform subsampling of a full spin acquisition (angular step is $\gamma = 30°$).

CBCT acquisition. For a maximum aperture of $60°$, a gap of $120°$ is not sampled. Pattern P_1 augments pattern P_0 with a single projection acquired with the lateral plane in a direction orthogonal to the central projection of P_0, so that gaps between projections never exceed $60°$. Pattern P_2 corresponds to the case where both planes would rotate simultaneouly, thus allowing for a complete tomographic coverage with uniform subsampling. The largest angular step that was tested was $30°$ amounting to acquiring 6 projections only. In terms of mechanical design, pattern P_2 implies the strongest requirements on the lateral plane: that it can rotate synchronously with and in the same repeatable way as the frontal plane, despite its rather different design. Pattern P_1 only requires reaching a single position precisely and repeatably. Pattern P_0 alleviates any constraint on the lateral plane.

B. Sparse iterative reconstruction through ℓ_1 minimization

Previous works have shown the possibility to handle subsampling using ℓ_1-constrained reconstructions, one in particular in the context of C-arm CBCT imaging of an iodined-injected sparse vessel tree over a non-sparse background [1]. C-arm CBCT imaging of coils falls into the same category. Following [1], we take a hierarchical approach where structures of higher intensity are reconstructed first. It is based on solving the following N penalized reconstruction problems indexed by n:

$$f^{(n)} = \underset{f \geq 0}{\operatorname{argmin}} \frac{1}{2}(Rf - p)^t D(Rf - p) + \lambda^{(n)}||f||_1 \qquad (1)$$

where R is a matrix that models the acquisition pattern, D is the matrix of ramp filtering, p is the vector of the projections acquired with the pattern, f is the vector containing the reconstructed volume and $\lambda^{(n)}$ is a positive scalar that defines the level of sparsity of the solution by acting as an intensity threshold. Vector $f^{(n)}$ is thus an approximation of the solution whose sparsity is proportional to $\lambda^{(n)}$. Since the coil sparsity is not known, N problems (called stages) is defined a priori with N intensity thresholds $\lambda^{(n)} \in [\lambda_{\min}, \lambda_{\max}]$ such that $\lambda^{(n)} \geq \lambda^{(n+1)}$ and $\lambda_{\min} > 0$. At each stage, $f^{(n)}$ is computed as the solution of (1) initialized by $f^{(n-1)}$ using proximal splitting, that is the following 2-step iterative algorithm:

$$\begin{cases} f^{(i+\frac{1}{2})} & = f^{(i)} - \tau R^t D(Rf^{(i)} - p) \\ f^{(i+1)} & = \operatorname{argmin}_{f \geq 0} ||f - f^{(i+\frac{1}{2}))}||^2 + \lambda^{(n)}||f||_1 \end{cases} \qquad (2)$$

To get matrix R to model each pattern we must consider the weighting of each projection. It is a single scaling factor when the sampling is uniform. When it is not, as in pattern P_1, it is intuitive that the projection from the lateral plane contains unique information. Indeed, we found necessary to give this extra-projection a weight equal to the sum of the weights of all other projections to get the best results.

C. Structural prior through diffusion filtering

Promoting curvilinear structures is introduced as a filtering operator W modifying (2) into the following 3-step algorithm:

$$\begin{cases} f^{(i+\frac{1}{3})} & = f^{(i)} - \tau R^t D(Rf^{(i)} - p) \\ f^{(i+\frac{2}{3})} & = W(f^{(i+\frac{1}{3})}) \\ f^{(i+1)} & = \operatorname{argmin}_{f \geq 0} ||f - f^{(i+\frac{2}{3}))}||^2 + \lambda^{(n)}||f||_1 \end{cases} \qquad (3)$$

Operator W is a diffusion filter such that the filtered image $f^{(i+\frac{2}{3})}$ is solution of the diffusion equation :

$$\begin{cases} \partial_t f & = \nabla^t(T(f).\nabla f) \\ f(t=0) & = f^{(i+\frac{1}{3})} \end{cases} \qquad (4)$$

where ∇ denotes the gradient operator and T is a 3×3 matrix designed to locally modulate the strength and direction of the filtering according to the underlying structures in image f. Three designs of T are investigated :

- $T_{\text{CED}} = U_\theta \text{diag}(\lambda_{\text{CED}}, \alpha, \alpha) U_{-\theta}$ where U_θ is a rotation matrix such that the filtering has diffusivity λ_{CED} along direction θ. This corresponds to Weickert's Coherent-Enhancing Diffusion where U_θ and λ_{CED} are computed as described in [2]. We have $\alpha << 1$, that is no filtering in directions orthogonal to θ, and $\lambda_{\text{CED}} \in [\alpha, 1]$. We expect close to full filtering ($\lambda_{\text{CED}} \to 1$) when the underlying structure is curvilinear and close to no filtering ($\lambda_{\text{CED}} \to \alpha$) otherwise.
- $T_{\text{NLD}} = (1 - \lambda_{\text{CED}})\text{diag}(1, 1, 1)$ is an isotropic non-linear diffusion tensor based on λ_{CED} only which is expected to smooth out non-curvilinear structures while leaving curvilinear structures unchanged.
- $T_{\text{NLAD}} = U_\theta \text{diag}(\lambda_{\text{CED}}, 1 - \lambda_{\text{CED}}, 1 - \lambda_{\text{CED}}) U_{-\theta}$ is an anistropic non-linear diffusion tensor combining the two above designs such that curvilinear structures are enhanced and non-curvilinear structures are smoothed out.

III. Experiments

We present results on one coil in air and four clinical data sets obtained right after the first coil was deployed within the aneurysm sack. All five data sets were acquired with the same GE Healthcare IGS 630 biplane C-arm system, following a standard workflow of CBCT spin acquisition (pixel pitch 0.4mm, rotation speed $40°$/s, 150 projections total). The acquisition patterns were derived by extracting the projections from

the full spin. Subsets of projections $P_0(\alpha,\theta)$ were generated following pattern P_0 for eleven values of the aperture angle α from 30° to 60° in steps of 3° and four values of the start angle θ of the rotation from 0° to −30° in steps of 10°. For each subset $P_0(\alpha,\theta)$, a corresponding subset $P_1(\alpha,\theta)$ following pattern P_1 was obtained by adding an orthogonal projection as described in Sec. II-A. Subsets $P_2(\gamma)$ were generated following pattern P_2 for increasing angular steps γ, starting from the ground truth (GT) of 150 projections ($\gamma = 1.5°$) down to as low as 6 projections ($\gamma = 30°$). Fig.2 shows configuration $P_1(60°,0°)$ and $P_2(30°)$. All ℓ_1-constrained reconstructions, including ground-truth reconstructions of full spins, were performed with the same parameters: $N = 30$, $f^{(0)} = 0$, $\lambda_{\max} = 0.9 \times \max(f^{(1/2)})$ where $f^{(1/2)}$ is a least-square approximation of f, $\lambda_{\min} = 3000$ to separate the coil from other intense anatomical structure (eg. bones). Since we are interested in recovering the shape of the coil (ie its loops), reconstructions were evaluated quantitatively in terms of support only. Let $f^{(01)}$ denote the binarized version of the soft-background thresholded volume $f^{(N)}$. The false negative (FN) rate is defined as the proportion of non-zero voxels of the ground-truth reconstruction of the coil ("true voxels") that are missing in $f^{(01)}$ with respect to the total number of true voxels. The false positive (FP) rate is defined as the proportion of non-zero voxels appearing in $f^{(01)}$ that are not true voxels with respect to the total number of true voxels. The FN (resp. FP) rate best value is 0%. The max value for the FN rate is 100% but can exceed 100% for the FP rate. For settings $P_1(60°,0°)$ and $P_2(30°)$, reconstructions were also performed using the diffusion filters of Sec. II-C. We compared using algorithm (3) at all stages of the hierarchical approach to using algorithm (2) from stages 1 to $N-1$ and algorithm (3) at the last stage N. This latter approach is faster because it uses diffusion essentially as a post-processing step. Filtering impact was quantified as the (signed) percentage of improvement in FN (resp. FP) rates with respect to no filtering defined by : $100 \times (\text{FN}_{\text{Filter}} - \text{FN}_{\text{NoFilter}})/\text{FN}_{\text{NoFilter}}$ (resp. $100 \times (\text{FP}_{\text{Filter}} - \text{FP}_{\text{NoFilter}})/\text{FP}_{\text{NoFilter}}$).

IV. Results

Fig.3 shows a scatter plot of the FN and FP rates of each setting $P_1(\alpha,0°)$ and $P_2(\gamma)$ (one dot per reconstruction). The plots compare patterns P_1 (blue symbols, one symbol per aperture angle α) and P_2 (red symbols, one symbol per angular step γ) for the clinical data combining all 4 patients. We observe very different plot trends between patterns P_1 and P_2. Pattern P_1 curves have a vertical trend, with the FN rate decreasing as the aperture increases with little increase of the FP rate except for patient 4. The same trend was found for pattern P_0 (not shown on plot), with higher FN rates than pattern P_1. With pattern P_2, the FN rate was always lower than with pattern P_1 while the subsampling implied increased FP rate. The two plots of Fig.4 show the influence of the starting angle θ for pattern P_1 for the ex-vivo coil (Fig.4a) and patient 2 (Fig.4b) data. The best starting angle for the ex-vivo coil ($\theta = -30°$) is the worst for the patient case, for which

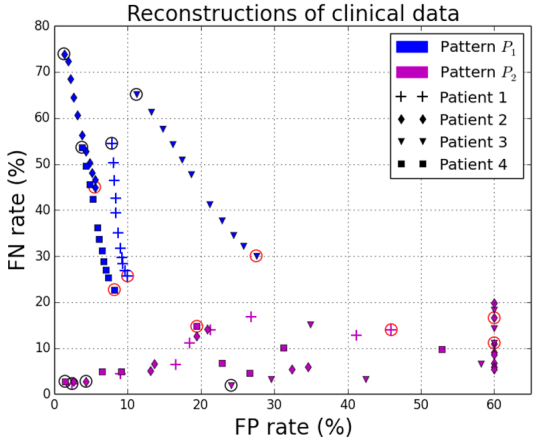

Fig. 3. FN rates against FP rates (clipped to 60%) comparing P_1 and P_2. Black circles : $P_1(30°,0°)$, $P_2(3°)$. Red circles : $P_1(60°,0°)$, $P_2(30°)$.

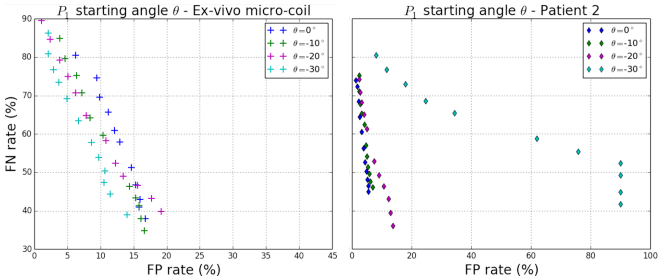

(a) (b)

Fig. 4. Plots of FN rates against FP rates (4b clipped to 90%) showing the impact of the starting angle θ for pattern P_1.

more variability is observed, possibly due to the presence of more intense background structures. Overall, systematically lower FN rates are obtained with pattern P_2 showing a better recovery of the coil in reconstructions than those obtained with pattern P_1, but at the cost of higher FP rates yielding visually noisier reconstructions. Visual inspection of the coil reconstructions as MIP rendering images for patient 1 and patient 2 are provided. A comparison of the ground truth (GT) reconstruction with reconstructions obtained with each pattern of Fig.2 and using algorithm (2) at all stages of the hierarchical approach is provided on Fig.5. Visual quality of the reconstruction is ranked lowest for P_0 (Fig.5b) and highest for P_2 (Fig.5d). Result for P_1 (Fig.5c) shows that using one extra-projection orthogonal to the center orientation of P_0 significantly improves the quality of the reconstruction. The GT reconstruction for patient 2 shows a peripheral loop of the coil (see arrow) on Fig.6a. This key clinical information is not entirely recovered with P_1 whatever the starting angle θ (Fig.6b,6c,6e,6f). It is clearly recovered using $P_2(30°)$ (Fig.6d) ie with 6 projections only. Quantitative results where 3D diffusion filtering of settings $P_1(60°,0°)$ and $P_2(30°)$. TABLE I reports the percentage of improvement for FN and FP rates averaged over all four clinical data sets. Overall, multi-directional diffusion tensors T_{NLAD} and T_{NLD} had more

impact than T_{CED}. Using diffusion as a post-processing (algorithm (3) at stage N only) generally resulted in better FN and FP rates than using diffusion at all stages of the hierarchical approach. Diffusion filtering with T_{NLAD} reduced the structural noise induced by angular subsampling (decreased FP rates) and recovered some of the missing information (decreased FN rates). It is most significant with pattern P_2 where there is more structural noise than with pattern P_1. Fig.7 shows reconstructions obtained using diffusion at all stages of the hierarchical approach for patient 1 with setting $P_2(30^\circ)$. Coherence enhancing diffusion filter (T_{CED} tensor) resulted in visually smoother coil structures (Fig.7a) with some remaining structural noise. The alternative isotropic tensor T_{NLD} resulted in visually less noisy reconstructions (Fig.7b) while tensor T_{NLAD} appears to produce a good combination of the other two filters (Fig.7c).

V. Discussion and Conclusion

In this paper we evaluated three subsampled rotational acquisition patterns for intra-operative 3D coil imaging that are specifically designed for biplane C-arm systems. Sparse approximation through ℓ_1-constrained reconstruction was used to generate 3D images of the coil in presence of missing projection data. Results obtained for one coil in air and four patient datasets showed how a sparse approximation performs according to both the selected acquisition pattern and the quantity of missing information (angular aperture or angular step) in terms of support recovery and visual inspection. Analysis of false negative and true positive rates clearly distinguished the limited aperture patterns P_0 and P_1 from the uniformly subsampled pattern P_2. Pattern P_0 was deemed insufficient in all cases, and pattern P_2 was ranked best. In between, pattern P_1 showed a non-negligible variability depending on the start angle of the acquisition. This confirms that there exists a preferred direction in which a coil should be imaged, as described in a different context by Varga [3], in order to avoid unfavorable background superimposition. Indeed, we found in one instance that a clinically important information was not recovered with pattern P_1 whatever the starting angle. Pattern P_2 was able to recover this information with as few as 6 projections. We also investigated using 3D diffusion filtering as part of the reconstruction process to promote curvilinear structures. Three different diffusion tensor designs were considered to locally modulate the strength and direction of the filtering. All three filters improved the reconstructions either by promoting curvilinear structure and/or smoothing out structural noise.

References

[1] H. Langet, C. Riddell, A. Reshef, Y. Trousset, A. Tenenhaus, E. Lahalle, G. Fleury, and N. Paragios, "Compressed-sensing-based content-driven hierarchical reconstruction: Theory and application to c-arm cone-beam tomography," *Medical Physics*, vol. 42, no. 9, pp. 5222–5237, 2015.

[2] J. Weickert, *Anisotropic diffusion in image processing*, vol. 1.

[3] L. Varga, P. Balázs, and A. Nagy, "Projection selection dependency in binary tomography." *Acta Cybern.*, vol. 20, no. 1, pp. 167–187, 2011.

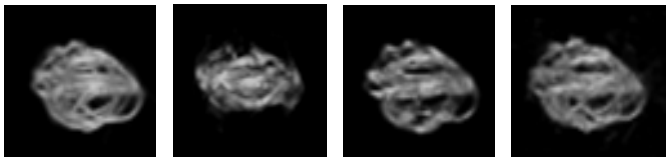

(a) (b) (c) (d)

Fig. 5. Patient 1. MIP rendering of reconstructions without diffusion filtering: (a) GT, (b) P_0 $(60^\circ, 0^\circ)$, (c) P_1 $(60^\circ, 0^\circ)$, (d) P_2 (30°).

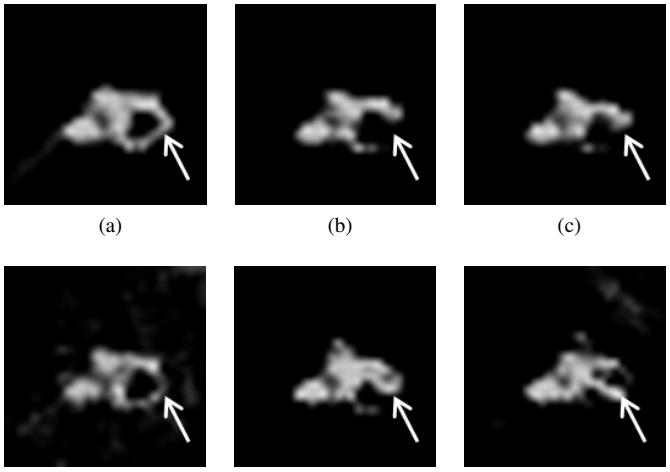

(a) (b) (c)

(d) (e) (f)

Fig. 6. Patient 2. MIP rendering of reconstructions without diffusion filtering: (a) GT, (d) P_2 (30°), (b) P_1 $(60^\circ, 0^\circ)$, (c) P_1 $(60^\circ, -10^\circ)$, (e) P_1 $(60^\circ, -20^\circ)$, (f) P_1 $(60^\circ, -30^\circ)$. White arrow points at a coil loop.

TABLE I
Comparing % improvement of FN and FP rates using diffusion filtering at all stages or last stage only for acquisition patterns $P_1(60^\circ, 0^\circ)$ and $P_2(30^\circ)$

Diffusion tensor T	P_1, all		P_1, last		P_2, all		P_2, last	
	FN	FP	FN	FP	FN	FP	FN	FP
CED	-1	$+3$	-2	-2	$+4$	-11	-4	-14
NLD	-7	$+5$	-6	-8	-22	-27	-24	-28
NLAD	-4	$+2$	-8	-11	-19	-31	-27	-29

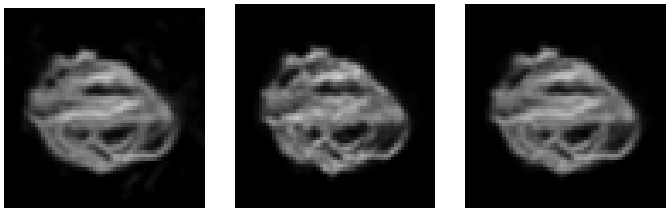

(a) (b) (c)

Fig. 7. Patient 1. MIP rendering of reconstructions with diffusion filtering at all stages and pattern P_2 (30°): (a) CED, (b) NLAD